



**HAL**  
open science

# Digital image correlation analyses of masonry infilled frame: Uncertainty-based mesh refinement and damage quantification

Vinicius Fiocco Sciuti, Rafael Vargas, Nestor Guerrero, María Eugenia Marante, François Hild

## ► To cite this version:

Vinicius Fiocco Sciuti, Rafael Vargas, Nestor Guerrero, María Eugenia Marante, François Hild. Digital image correlation analyses of masonry infilled frame: Uncertainty-based mesh refinement and damage quantification. *Mathematics and Mechanics of Solids*, 2024, 10.1177/10812865231174840 . hal-04079689

**HAL Id: hal-04079689**

**<https://hal.science/hal-04079689v1>**

Submitted on 24 Apr 2023

**HAL** is a multi-disciplinary open access archive for the deposit and dissemination of scientific research documents, whether they are published or not. The documents may come from teaching and research institutions in France or abroad, or from public or private research centers.

L'archive ouverte pluridisciplinaire **HAL**, est destinée au dépôt et à la diffusion de documents scientifiques de niveau recherche, publiés ou non, émanant des établissements d'enseignement et de recherche français ou étrangers, des laboratoires publics ou privés.

---

# Digital image correlation analyses of masonry infilled frame: Uncertainty-based mesh refinement and damage quantification

Journal Name  
XX(X):1-??  
©The Author(s) 2022  
Reprints and permission:  
sagepub.co.uk/journalsPermissions.nav  
DOI: 10.1177/ToBeAssigned  
www.sagepub.com/

SAGE

Vinicius Fiocco Sciuti,<sup>1</sup> Rafael Vargas,<sup>2,3</sup> Néstor Guerrero,<sup>4</sup> María Eugenia Marante<sup>5</sup> and François Hild<sup>3</sup>

## Abstract

Masonry walls are subjected to cyclic lateral loads to study damage caused by earthquakes. Imaging techniques are useful to quantify crack networks in such tests, where preferential locations for their initiation are not present. However, detecting small cracks in large structures is challenging. It is shown that FE-based digital image correlation (DIC) can detect and quantify cracks by combining optical and mechanical information of a cyclic shear experiment performed on a full-size masonry wall. Pixel-wise gray level residuals and elementary crack opening displacement fields are the key quantities of the proposed framework. Detection criteria based on standard uncertainties guided the application of new DIC strategies (*i.e.*, mechanical regularization, mesh adaption, and damage). Two damage regimes were quantified. Zigzagged cracks were first formed for which their opening displacements were on average less than 0.5 mm with very limited damage. They were followed by sliding shear cracks whose mean opening displacements varied between 1 and 3 mm, and damage developed in a more gradual and extended way. Such rich full-field dataset may be used for validating damage models up to full scale simulations.

## Keywords

Adapted mesh, crack opening displacement, digital image correlation (DIC), full-scale experiment, mechanical regularization

## Introduction

Masonry infilled frames are the structural system most used in low-income housing in Latin American countries due to the accessibility of the materials and simplicity of construction. Most of these countries lie in areas with moderate to high seismic hazards. Almost always, these constructions were built without any structural analysis or design, thus the structural performance under different types of load histories they may be subjected remains uncertain. It is thus desirable to have models to perform numerical simulations of masonry structures, for instance macromodels accounting for damage initiation and growth. Using these models, essential features observed in experiments should be reproduced (*e.g.*, shear strength, strain levels, and cracking patterns of confined and unconfined masonry panels).<sup>1-4</sup>

Different Latin American countries have adopted in their analysis and design codes, criteria mainly based on ultimate

---

<sup>1</sup>Federal University of São Carlos (UFSCar), Department of Materials Engineering (DEMa), São Carlos-SP, Brazil

<sup>2</sup>Federal University of São Carlos, Graduate Program in Materials Science and Engineering (PPGCEM), São Carlos-SP, Brazil

<sup>3</sup>Université Paris-Saclay, CentraleSupélec, ENS Paris-Saclay, CNRS, LMPS - Laboratoire de Mécanique Paris-Saclay, Gif-sur-Yvette, France

<sup>4</sup>Department of Civil Engineering, Universidad of Ibagué, Ibagué, Colombia

<sup>5</sup>Construction and Sustainable Development Department, Universidad Metropolitana, Caracas, Venezuela

## Corresponding author:

François Hild, Université Paris-Saclay, LMPS - Laboratoire de Mécanique Paris-Saclay, 91190 Gif-sur-Yvette, France.

Email: francois.hild@ens-paris-saclay.fr

limits,<sup>5–10</sup> considering various failure modes. However, these criteria remain an active research topic in order to improve the reliability of such structures. The current literature offers extensive information on experiments geared toward the identification of failure modes, strength, stiffness, and other structural parameters to calibrate models to run numerical simulations for the analysis and design of buildings with this type of structural systems. Asteris et al.<sup>11</sup> classified the failure modes observed experimentally in simple shear into the five categories schematically shown in Figure 1.

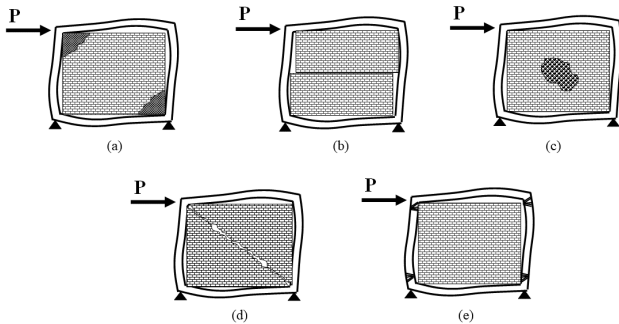


**Figure 1.** Different failure modes of masonry-infilled frames subjected to simple shear. (a) Corner crushing mode; (b) sliding shear mode; (c) diagonal compression mode; (d) diagonal cracking mode; (e) frame failure mode (adapted from Ref.<sup>12</sup>).

The approaches for modeling the behavior of infilled frames are divided into two groups, namely, micro- and macro-models.<sup>13</sup> In micromodels, the masonry is represented as a continuum discretized into numerous finite elements. This approach gives rich descriptions of the phenomena taking place in the infill under overloads including the interface between frames and infill. In macromodels, the infill is usually substituted by a single, or a set of diagonal struts. The micromodels intend to consider all possible failure modes, but their use is limited to very simple structures due to the complexity of the analysis and the large amount of data that are collected. For large structures such as buildings, macromodels are usually chosen. Very simple and schematic results are obtained yet they are considered accurate enough for engineering purposes.

Petry and Beyer<sup>14</sup> indicated that to improve the performance-based evaluation of buildings with unreinforced masonry, future research should focus on the development of models that relate the global force-displacement response to local deformations of the considered elements. The authors proposed two sets of limit states that link localized damage to characteristic points in the global force-displacement response of unconfined masonry. Deformation

measurements at the brick level were performed with an LED-based optical system. An alternative route consists in utilizing Digital Image Correlation (DIC).<sup>15</sup> DIC was used to measure motions of large scale structures such as bridges.<sup>16,17</sup> In the following, it will be used to detect and quantify two damage mechanisms at the microscale of a masonry infilled frame subjected to confined shear.

The feasibility of DIC analyses for the analysis of brick walls was shown by Tung et al.<sup>18</sup> by reporting displacement and strain fields. A lot of emphasis was put on the use of the equivalent von Mises strain. Later on, it was also suggested that major eigen strain fields were more suited for the visualization of damage<sup>4,19–27</sup> and the analysis of various damage mechanisms in masonry.<sup>12,28,29</sup> Other strain components were also considered depending on the investigated experiment.<sup>18,30</sup> Bolhassani et al.<sup>31</sup> defined structural cracks as zones in which the strain levels were greater than 0.3%. It was also shown DIC was crucial in other aspects associated with boundary conditions and calibration of mechanical parameters.<sup>32</sup>

Guerrero et al.<sup>12</sup> used DIC for evaluations of simplified models of infilled framed structures. Two different deformation mechanisms were found, namely, diagonal cracking (Figure 1(d)) during hardening phases and sliding shear during softening stages (Figure 1(b)). The inclination of the bands depended on the brick dimensions and arrangement. Didier et al.<sup>33</sup> quantified two proposed damage scores using DIC. Korswagen et al.<sup>34</sup> used DIC to detect crack formation and the evolution of the crack pattern, to calibrate and validate nonlinear finite element models. The authors defined a damage parameter as a function of the number, length and width of cracks in masonry walls. In the following analyses, two other damage indicators will be introduced.

Ghorbani et al.<sup>28</sup> performed uncertainty quantifications and validated DIC readings against point-wise sensors for experiments on full-scale masonry walls. Attempts were made to evaluate crack widths from displacement fields as previously proposed by Fedele et al.<sup>32</sup> Other studies followed along the same direction.<sup>34–36</sup> More recently, systematic damage quantification was performed when analyzing eigen strain fields. Detection threshold were introduced with arbitrary levels<sup>37</sup> or based on measurement uncertainties.<sup>38</sup> Uncertainty levels will be utilized hereafter to adapt the mesh in FE-based DIC, and to detect damaged elements.

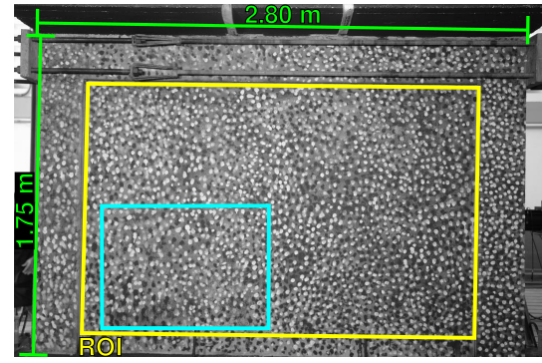




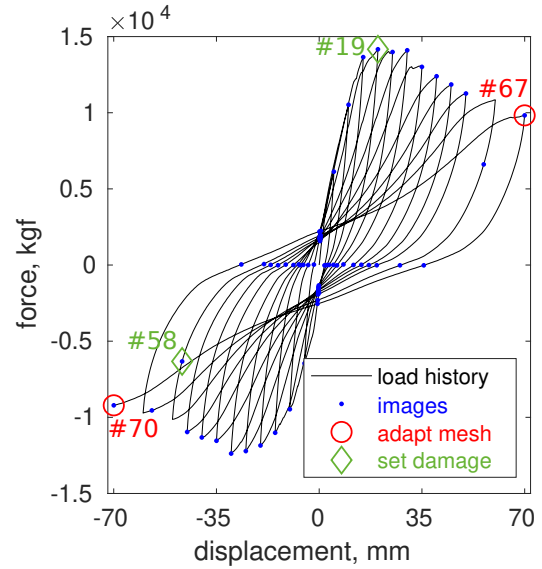
**Figure 3.** Masonry infilled frame before the experiment. The hydraulic actuator is shown in the dashed red box. The 50 kN dead load is visible above the frame.

Figure 4(a) shows the acquired image of the reference configuration with the Region Of Interest (ROI) for DIC purposes depicted as a yellow box. To achieve good contrast for DIC purposes, the speckle pattern (Figure 3) was made first with a thin layer of black paint to emphasize the texture of the cladding. Black dots were then painted, and last yellow dots over the former. The hardware parameters are gathered in Table 1.

The applied displacement and resulting force are shown in Figure 4(b). One reference image was acquired prior to loading and 70 at the peak load of each cycle and when force or displacement were canceling out.



(a)



(b)

**Figure 4.** (a) Reference image of the unloaded configuration with the ROI highlighted in the yellow box. The smaller cyan box is discussed in Figure 14. (b) Loading history in which the blue dots depict image acquisitions. The red circles highlight the images used for adapting the meshes and the green diamonds those utilized for setting the damage parameter.

### DIC framework

*FE-based registrations* All the DIC analyses were performed with the Correli 3.0 framework,<sup>47</sup> and the selected parameters are summarized in Table 2. Brightness conservation was considered

$$f(\mathbf{x}) = g(\mathbf{x} + \mathbf{u}(\mathbf{x})) \quad (1)$$

for each pixel  $\mathbf{x}$  in the reference image  $f$  (of the unloaded state, see Figure 4(a)) and in deformed (state) corresponding to image  $g$  where a displacement  $\mathbf{u}$  has occurred. The displacement fields are discretized using 3-noded (T3) elements whose shape functions are  $\Psi_i^{T3}$ . The corresponding nodal displacements  $v_i$ , which are gathered in the column vector  $\{\mathbf{v}\}$  are determined via non-linear least squares

minimization of the global gray level residual  $\varrho$

$$\varrho^2(\{\mathbf{v}\}) = \sum_{ROI} [f(\mathbf{x}) - g(\mathbf{x} + \sum_i v_i \Psi_i^{T3}(\mathbf{x}))]^2 \quad (2)$$

by iteratively solving linear systems of the form  $[\mathbf{H}]\{\delta\mathbf{v}\} = \{\mathbf{h}\}$ , in which  $\{\delta\mathbf{v}\}$  is the vector of nodal displacement corrections,  $[\mathbf{H}]$  the Hessian matrix

$$H_{ij} = \sum_{ROI} (\Psi_i^{T3} \cdot \nabla f)(\mathbf{x})(\Psi_j^{T3} \cdot \nabla f)(\mathbf{x}) \quad (3)$$

and  $\{\mathbf{h}\}$  the right-hand member

$$h_i = \sum_{ROI} [f(\mathbf{x}) - \tilde{g}(\mathbf{x})](\Psi_i^{T3} \cdot \nabla f)(\mathbf{x}) \quad (4)$$

with  $\tilde{g}$  the corrected image  $g$  by the current estimate of the displacement field  $\tilde{\mathbf{u}}$ ,  $\tilde{g}(\mathbf{x}) = g(\mathbf{x} + \tilde{\mathbf{u}}(\mathbf{x}))$ . The normalized pixel-wise gray level residuals are thus defined as

$$\rho(\mathbf{x}) = \frac{f(\mathbf{x}) - \tilde{g}(\mathbf{x})}{\Delta f} \quad (5)$$

where  $\Delta f$  is the dynamic range of the reference picture (*i.e.*,  $\max(f) - \min(f)$ ).

Once convergence is achieved, the elementary strains are obtained by exact differentiation of the shape functions. Usually, the maximum eigen strain  $\epsilon_1$  is used to quantify crack networks<sup>12,37,38</sup> independently of their orientation or cracking mode. The Mean Crack Opening Displacement (MCOD) per element is calculated from the mean strain tensor estimated for each element  $e$  covering a domain  $\Omega_e$ .<sup>48</sup> In the presence of cracks, the mean strain tensor is expressed as<sup>49</sup>

$$\bar{\epsilon} = \frac{1}{|\Omega_e|} \int_{\Omega_e} \epsilon(\mathbf{x}) d\mathbf{x} + \frac{1}{|\Omega_e|} \int_{\Gamma_e} [\mathbf{u}(\mathbf{x})] \boxtimes \mathbf{n}(\mathbf{x}) ds \quad (6)$$

where  $[\mathbf{u}]$  denotes the displacement jump,  $\mathbf{n}$  the normal to the cracked surface  $\Gamma_e$ ,  $\boxtimes$  the symmetrized tensorial product,  $\epsilon$  the strain tensor of the uncracked matrix, and  $s$  the curvilinear abscissa along the crack path. In the following equations, it is assumed that the elastic strain levels are negligible in comparison to the singular contribution provided by cracks. Consequently, the mean strain tensor becomes

$$\bar{\epsilon} \approx \frac{1}{|\Omega_e|} \int_{\Gamma_e} [\mathbf{u}(\mathbf{x})] \boxtimes \mathbf{n}(\mathbf{x}) ds \quad (7)$$

The MCOD  $\overline{[u]}$  per finite element is defined as

$$\overline{[u]} \boxtimes \bar{\mathbf{n}} = \frac{1}{|\Gamma_e|} \int_{\Gamma_e} [\mathbf{u}] \boxtimes \mathbf{n} ds \quad (8)$$

where  $\bar{\mathbf{n}}$  is the mean crack normal. The average maximum principal strain  $\bar{\epsilon}_1$  is then related to the equivalent MCOD

$$|\Omega_e| \bar{\epsilon}_1 = |\Gamma_e| \overline{[u]} \quad (9)$$

that accounts for both mode I and II contributions. It is worth noting that  $|\Omega_e|/|\Gamma_e|$  scales with the element size  $\ell$ , provided only one crack is present in each element. This is likely to be true for small element sizes. Consequently, the MCOD is approximated by

$$\overline{[u]} = \ell \bar{\epsilon}_1 \quad (10)$$

*Mechanical regularization* Mechanical regularization,<sup>50,51</sup> which is based on the equilibrium gap,<sup>52</sup> was used to help convergence in the present case. Considering that no internal forces should be present if the sample obeys linear elasticity, the regularization scheme changes the system to be solved to  $[\mathbf{H}^t]\{\delta\mathbf{v}\} = \{\mathbf{h}^t\}$ , in which

$$[\mathbf{H}^t] = [\mathbf{H}] + \omega_m \frac{\{\mathbf{v}\}^T [\mathbf{H}] \{\mathbf{v}\}}{\{\mathbf{v}\}^T [\mathbf{K}]^T [\mathbf{K}] \{\mathbf{v}\}} [\mathbf{K}]^T [\mathbf{K}] \quad (11)$$

and

$$\{\mathbf{h}^t\} = \{\mathbf{h}\} - \omega_m \frac{\{\mathbf{v}\}^T [\mathbf{H}] \{\mathbf{v}\}}{\{\mathbf{v}\}^T [\mathbf{K}]^T [\mathbf{K}] \{\mathbf{v}\}} [\mathbf{K}]^T [\mathbf{K}] \{\tilde{\mathbf{v}}\} \quad (12)$$

where  $[\mathbf{K}]$  is the stiffness matrix,  $\{\mathbf{v}\}$  the nodal displacements associated with a trial displacement field described by a plane wave,  $\{\tilde{\mathbf{v}}\}$  the vector containing the current estimate of the nodal displacements, and  $\omega_m$  the weight, which is related to regularization length  $L_{reg}$  by  $\omega_m \propto L_{reg}^4$ . In this paper,  $L_{reg} = 0$  and  $L_{reg} = 50$  px were selected and compared for highlighting the interest of the discussed methodology. The 50-px length was chosen as a compromise between measurement uncertainty and not filtering out too much high frequency displacements. The interested reader is referred to Refs.<sup>51,53</sup> for additional details on the implementation of such regularization schemes.

*Hanging nodes* The mesh considered hereafter will not be uniform, contrary to classical practice.<sup>39,50</sup> It will be adapted according to a criterion based on the mean crack opening displacement<sup>41</sup> and its corresponding uncertainty that is assessed for each element. Nodes with a reduced number of connectivities, also called hanging nodes,<sup>41,54</sup> were generated during the refinement steps. Lagrange multipliers were used to prescribe the displacement of each hanging node to that of its adjacent nodes. For instance, the displacement of a hanging node in the middle of an edge is the mean value of the displacement of the two adjacent nodes. This approach was implemented in the DIC code by concatenating an auxiliary Lagrange matrix  $[\mathbf{L}]$  to the Hessian matrix  $[\mathbf{H}^t]$ , thereby generating an augmented Hessian matrix  $[\mathbf{H}^a]$

$$[\mathbf{H}^a] = \begin{bmatrix} [\mathbf{H}^t] & h[\mathbf{L}]^T \\ h[\mathbf{L}] & [\mathbf{0}] \end{bmatrix} \quad (13)$$

where  $h$  is the ratio of the Frobenius norms of  $[\mathbf{H}^t]$  and  $[\mathbf{L}]$  to avoid degrading the conditioning of the full system

$$[\mathbf{H}^a]\{\delta\boldsymbol{\beta}\} = \{\mathbf{h}^a\} \quad (14)$$

composed of a vector of unknowns  $\{\boldsymbol{\beta}\}$  containing nodal displacements and Lagrange multipliers, and the augmented residual vector  $\{\mathbf{h}^a\}$

$$\{\mathbf{h}^a\}^\top = \{\{\mathbf{h}^t\}^\top \{\mathbf{0}\}^\top\} \quad (15)$$

A detailed discussion of this approach is given in Ref. <sup>41</sup>

### Uncertainty quantification with uniform meshes

Only one reference image (*i.e.*, taken in the unloaded state) was available (Figure 4(a)). Since the gray level residual from the DIC analysis of the first pair of images was essentially associated with white Gaussian noise, 100 new reference images were created by adding Gaussian white noise (*i.e.*, standard deviation equal to 4.2 gray levels) to the reference image. Then, the uncertainties for displacements, strains, and MCODs were assessed by taking the standard deviation of the values measured in this set of images. If several images of the unloaded state had been available, the uncertainty analysis would have been directly conducted on them as is current practice <sup>42–44</sup>.

First, uniform meshes were considered, starting with an element size  $\ell = 560$  px, which was divided by two each time as shown in Figure 5. This analysis allows the thresholds to be set for adapting the mesh to better capture the crack pattern.

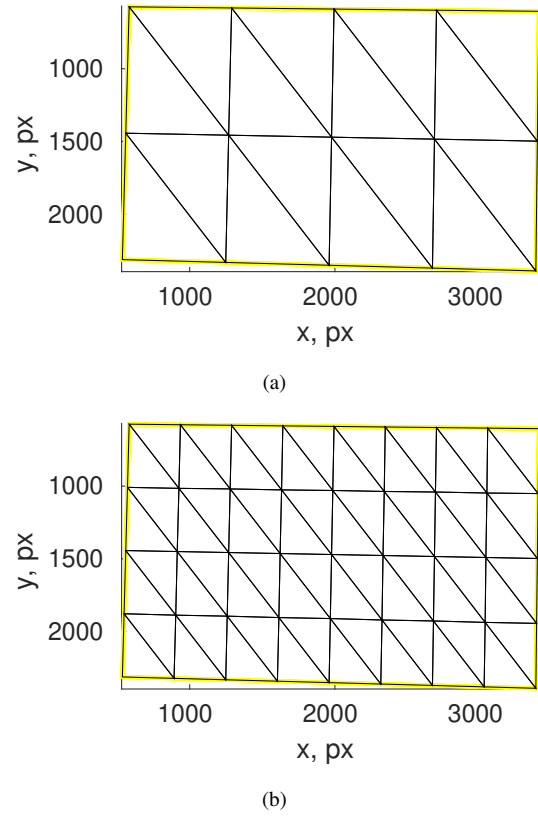


**Figure 5.** Uniform meshes with element lengths of 560 px (a) and 280 px (b). Each triangular element is divided into four new triangles. The physical size of one pixel is 790  $\mu\text{m}$ .

The standard uncertainties are shown in Figure 6 for the horizontal nodal displacements (Figure 6(a)), the major eigen strains (Figure 6(b)) and the MCOD (Figure 6(c)) as functions of the element size. When no mechanical regularization was used (*i.e.*,  $L_{reg} = 0$ ), the uncertainties decreased with an increase in element length. This trend is the well-known compromise between measurement uncertainty and spatial resolution. <sup>42</sup> Conversely, when mechanical regularization was used (*i.e.*,  $L_{reg} = 50$  px) the standard displacement uncertainties decreased for elements whose size was greater than the regularization length. For small elements, the displacement uncertainty was controlled by the regularization length and no longer by the element size.

The standard strain uncertainty had a dual decrease depending on the element size. This trend was due to the fact that the standard strain uncertainty was proportional to the standard displacement uncertainty divided by the element size. For MCODs, which again considered the element length in its calculation, the uncertainty was smaller than for small elements, further highlighting the interest of using such regularization scheme.

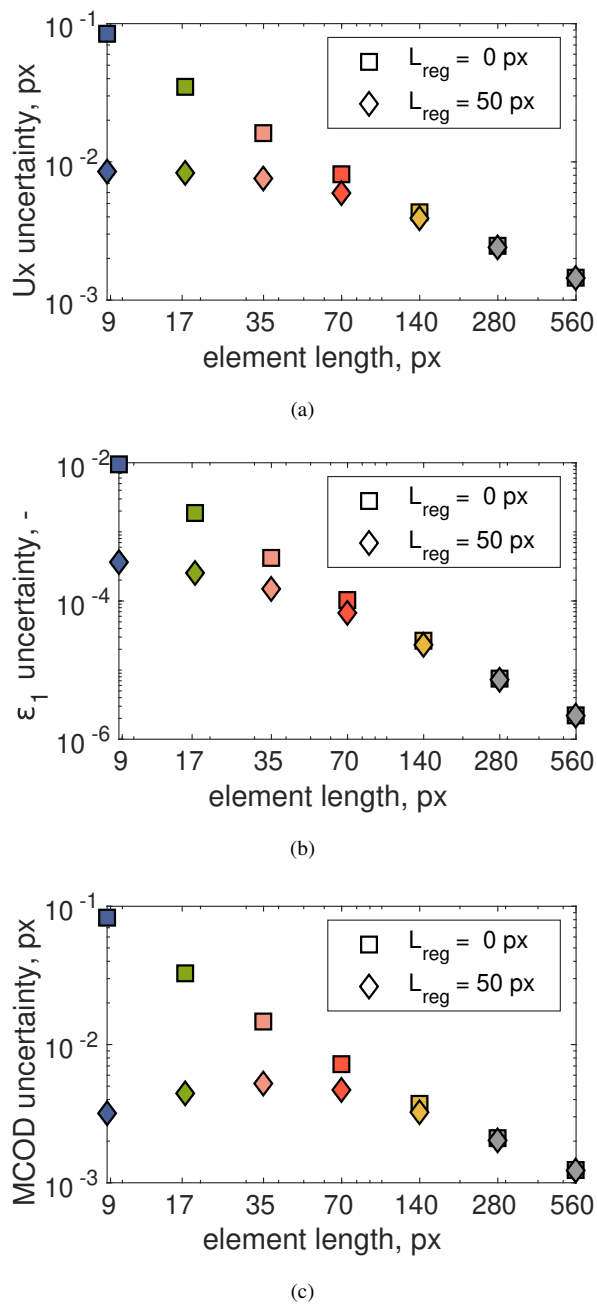


**Figure 6.** Standard uncertainties in terms of horizontal displacement (a), major eigen strain (b), and MCOd (c) for uniform meshes and two regularization lengths. The physical size of one pixel is 790  $\mu\text{m}$ .

The previous results illustrate the gains obtained with mechanical regularization as long as the regularization length is greater than the element size. When  $L = 50$  px, standard displacement *and* MCOd uncertainties less than  $10^{-2}$  px (or less than 8  $\mu\text{m}$ ) were achieved irrespective of the element size.

### Initial DIC results

The present case was very challenging for two main reasons. First, very high displacement amplitudes (*i.e.*, more than

100 px) were observed for some images of the cyclic test. Second, the wall cladding was also damaged as a result of the loading history (*i.e.*, significant deviations from gray level conservation). Therefore, some care had to be taken for the first DIC analysis that was used to initialize the subsequent procedures. A very coarse mesh with only 15 nodes (Figure 5(a)) was first used with no regularization. Moreover, an incremental approach was first run, meaning that the reference image and the nodal positions were updated for each new image to mitigate the influence of the changes in speckle pattern. This calculation was also initialized with a rigid body translation estimate using the cross-correlation product computed via fast Fourier transform.<sup>55</sup> It took at most 30 iterations (apart from the last frame) to converge for the norm of displacement increment to become less than  $10^{-3}$  px. In a direct analysis, it would have taken more than 200 iterations (or even diverge) if no proper initialization was performed.

To illustrate the result of this first analysis and to compare with the following ones, the final gray level residual for the most loaded state (with positive horizontal displacement) is shown in Figure 7(a). Although convergence was achieved, interpolation errors are visible, which call for more degrees of freedom to properly describe the complex kinematics near damaged regions. The standard deviation of all residual images is shown in Figure 7(b) normalized by the dynamic range (*i.e.*, 255 gray levels). For the first 18 images, a value of about 2% is seen, which is classical for DIC.<sup>56</sup> However, from image #19 onward, it increased very significantly; reaching almost 20%, due to damage of the wall and its cladding. Such levels illustrate the challenges faced in the analysis of the test.

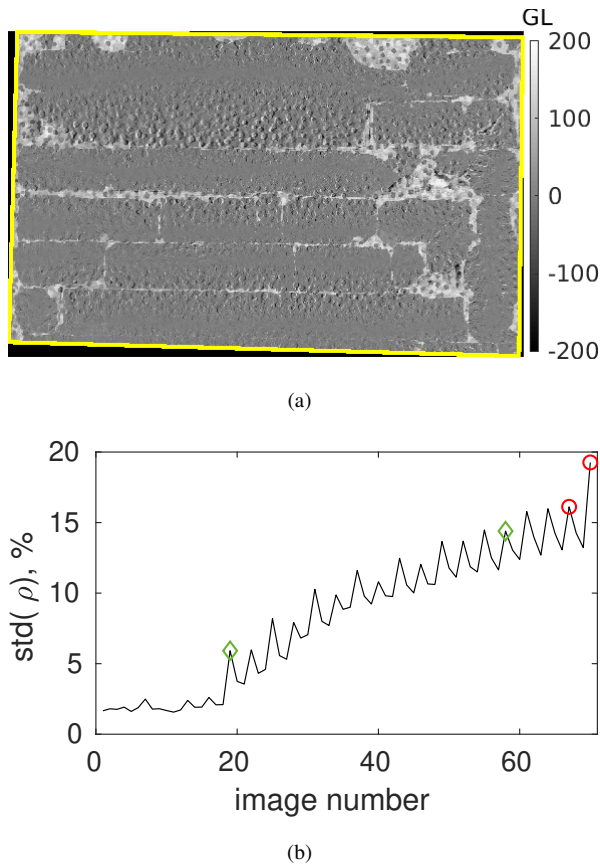


**Figure 7.** (a) Gray level residual for the initial DIC analysis using a coarse mesh (image #67). (b) Normalized standard deviation of gray level residuals (see Equation (5)). The green diamonds and red circles highlight images #19, 58, 67, and 70 further discussed in the text.

### Mesh adaption

Starting from the coarse discretization shown in Figure 5(a), the mesh was locally refined following the procedure described in Ref.<sup>41</sup> Each element is refined if the MCOD is greater than  $k$  times the standard uncertainty. For each step, the considered uncertainty was changed; it followed the estimates obtained for a uniform mesh ( $L_{reg} = 0$  px in Figure 6(c)). Six refinement steps were performed, which led to element sizes ranging from 9 px up to 560 px. Moreover, instead of using only one image for the deformed state as in Ref.<sup>41</sup>, two images were considered (*i.e.*, #67 and #70, see Figure 8), to account for both positive and negative prescribed displacements (Figure 4(b)). DIC analyses were run for each step using such images, and the elements were divided if the measured MCOD surpassed the threshold on any of these two results. This type of mesh adaption was tested for monotonically increasing crack openings and propagation.<sup>57</sup> In this work, due to the cyclic nature of the loading history, two systems of cracks were created, and

therefore the use of two images together for such procedure was tested (see Section “Crack network development”).

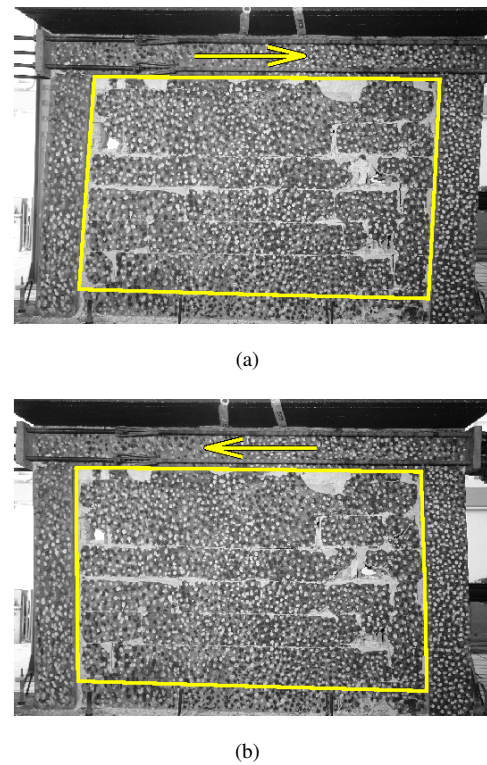


**Figure 8.** Images #67 and #70 of two deformed states that were used in the mesh adaption scheme (Figure 4(b)), respectively for the most loaded state with positive (a) or negative (b) displacements in the  $x$ -direction.

Different values of  $k$  were tested (*i.e.*,  $k = 1.5, 3, 6, 12$ ) and the resulting meshes are shown in Figure 9 with the colors depicting the size of the elements. Although the starting mesh had 560 px elements, the biggest element in the final mesh was 140 px in length (see top left corner in Figure 9) because all elements reached the MCOD threshold during the two initial adaption steps. Using the present methodology, a suitable mesh size was obtained with no need of user intervention. When selecting  $k = 1.5$  (Figure 9(a)), the results are too much affected by noise, with some very fine elements scattered throughout regions where no damage happened. Conversely,  $k = 12$  (Figure 9(d)) provided a coarser mesh that was not refined for many vertical cracks. Even if  $k = 6$  (Figure 9(c)) provided a suitable mesh for the following analyzes,  $k = 3$  (Figure 9(b)) was kept since it is suggested in Ref.<sup>41</sup> and showed the best compromise to refine the mesh closer to where damage occurred (*i.e.*, connected regions with high MCODs) while not being affected much by noise. It is worth noting that gray level residual per element could also have been used instead of the

MCOD fields,<sup>41</sup> which would help to localize nodes around the main cracks at the cost of losing information on smaller cracks. Such results are thus not reported hereafter.

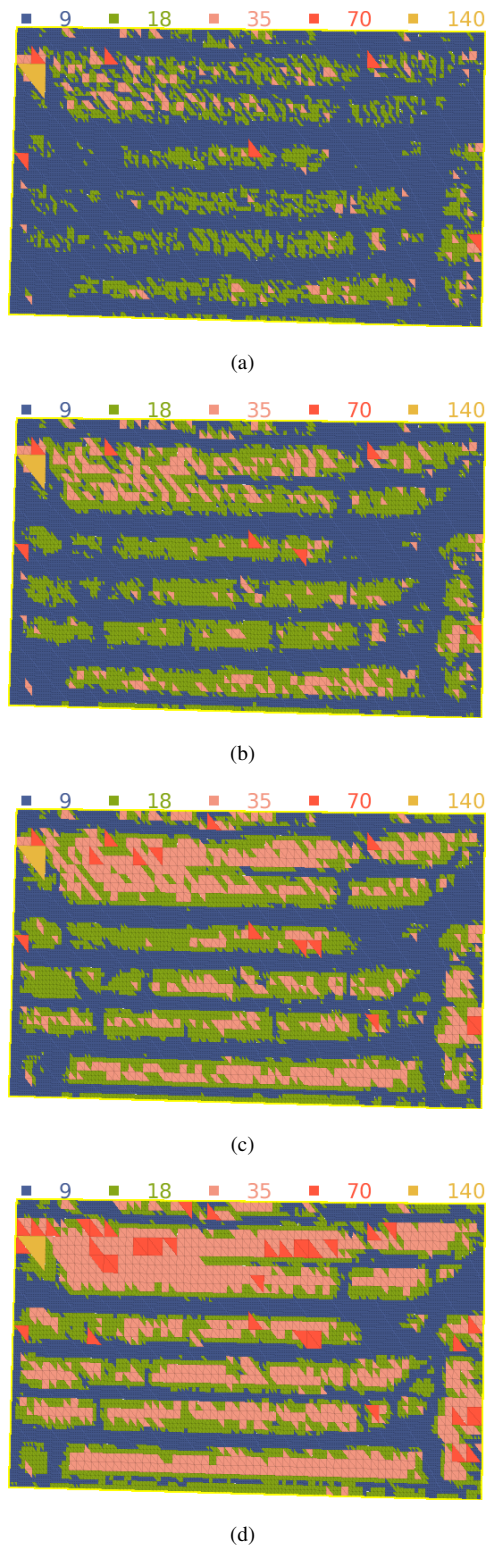


**Figure 9.** Adapted meshes using MCOD thresholds with  $k = 1.5$  (a),  $k = 3$  (b),  $k = 6$  (c), and  $k = 12$  (d). The colors depict the length of the elements expressed in px. The physical size of one pixel is  $790 \mu\text{m}$ .

Uncertainty analyses were then run using the adapted mesh shown in Figure 9(b) with the same set of 100 reference images as for the uniform meshes. Elements with same sizes were grouped to evaluate the corresponding uncertainties (Figure 10). The results are given for unregularized and regularized ( $L_{reg} = 50 \text{ px}$ ) DIC. For small element sizes with unregularized DIC, the MCOD uncertainties were close (*i.e.*, fell within error bars depicting the standard deviations of the standard uncertainties for the adapted mesh). The adapted mesh led to lower uncertainties as some small elements may have larger neighboring elements for which the uncertainty was lower. Conversely, for large element sizes, the trend was reversed due to the fact that large elements may have shared nodes with smaller adjacent elements.

Regarding mechanical regularization, the very same conclusions applied for the same reasons. However, the uncertainties were more dominated by the regularization length for smaller elements, which led to significantly lower levels in comparison with unregularized DIC. When  $L = 50 \text{ px}$ , standard displacement *and* MCOD uncertainties less than  $5 \times 10^{-3} \text{ px}$  (or less than  $4 \mu\text{m}$ ) were again achieved irrespective of the element size.

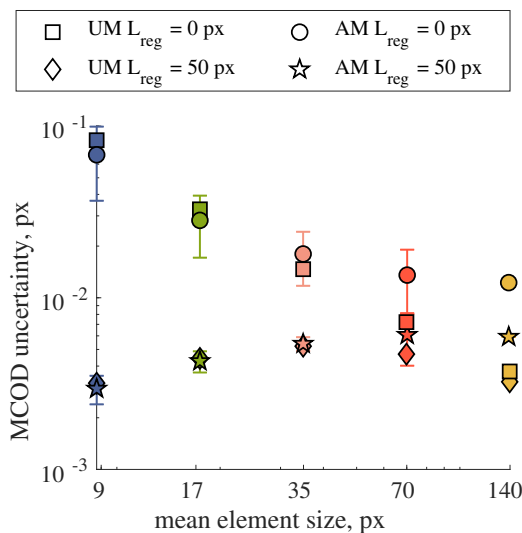


**Figure 10.** Standard MCOD uncertainties for the adapted mesh (AM, with  $k = 3$ , see Figure 9(b)) by groups of element size with no mechanical regularization or with  $L_{reg} = 50 \text{ px}$ . The mean standard uncertainties of each group are compared to the uncertainty of the uniform mesh (UM) with same element size. The error bar length depicts the standard deviations associated with the adapted meshes. The physical size of one pixel is  $790 \mu\text{m}$ .

The gray level residual image using the adapted mesh is shown in Figure 11 (to be compared with the results displayed in Figure 7). The areas with higher residuals are more localized in the cracked region. Far from them, the residual was considerably lower with no special pattern (*i.e.*, signature of noise). In some specific regions, it is possible to read the initial pattern in the residual since part of the wall cladding fell off and the background became white (see Figure 8).

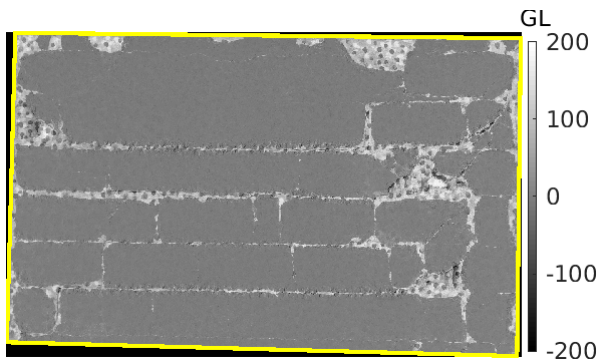
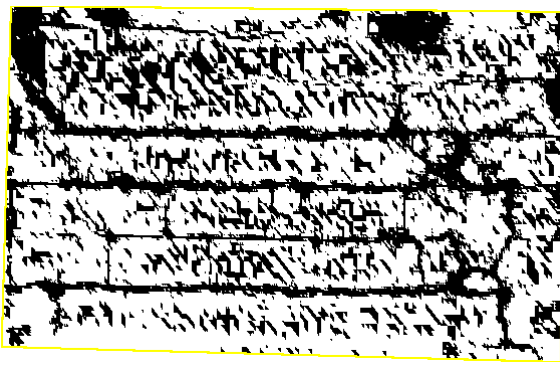


**Figure 11.** Gray level residual for the DIC analysis using the adaptive mesh (with  $k = 3$ , see Figure 9(b))

### Detection of Damage

Even though mesh adaption *per se* already gave a good description of the cracked regions, the use of mechanical regularization spread the strains around them.<sup>40</sup> Therefore, damage was added, leading to a relaxation of mechanical regularization locally in order to allow for higher displacement gradients. To choose which elements to damage (by multiplying its rigidity by  $(1 - D_0)$  with  $D_0 = 0.9$ ), three criteria were tested, namely, related to the MCOD, gray level residual, and both coupled. If, for a given image, the quantity of interest is higher than  $K$  times the uncertainty, the element is labeled damaged and its elementary stiffness matrix is degraded. All the following calculations were initialized with the one fully converged that used the adaptive mesh with no damage. The parameter  $D_0 = 0.9$  was selected to lower the regularization weight in damaged elements. This choice was motivated by two conflicting effects. If  $D$  is not high enough, it will be difficult to relocalize the strain and MCOD fields.<sup>40</sup> Conversely, given the fact that cladding loss was also observed (Figure 8), the damaged areas extended over many neighboring elements. If  $D$  was too high, it would have been impossible to achieve convergence of the DIC code.

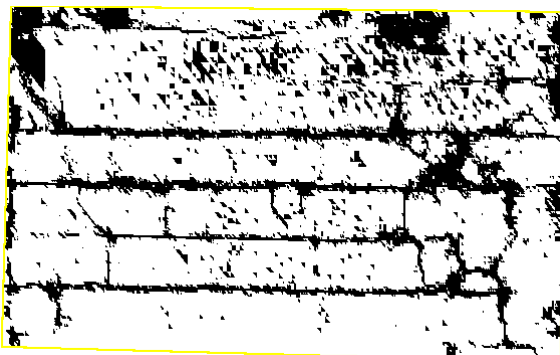
For the sake of simplicity, the first choice was to keep  $K = k = 3$  from the mesh adaption procedure. In the gray level residuals, the three approaches (*i.e.*, MCOD, gray level or coupled criterion) were indistinguishable. However, the damage fields were studied very carefully for deformed image #58 (Figure 4(b)). As shown in Figure 12 with  $K = 3$ , if only MCODs are used for the detection threshold (Figure 12(a)), some regions where no crack occurred were labeled as damaged. Further, if only the gray level residuals are used (Figure 12(b)), damage became affected by brightness and contrast changes during image acquisition. When both quantities are coupled (Figure 12(c)), the aforementioned effects were reduced and damage concentrated essentially on cracked regions. However, for all these three results, there were damaged elements at the very beginning of the analysis showing that  $K = 3$  was too low for such thresholds.



(a)



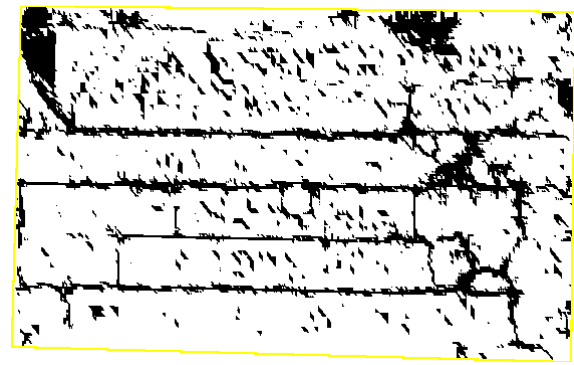
(b)



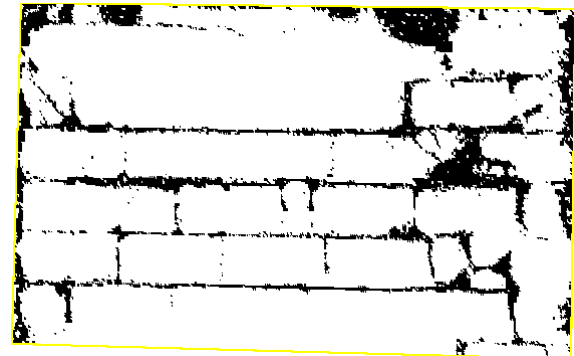
(c)

**Figure 12.** Damaged elements for deformed image #58 using as detection criterion only MCODs (a), gray level residuals (b), or both of them (c), all with  $K = 3$

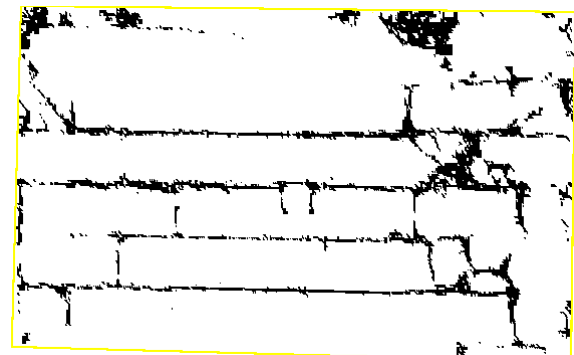
When testing  $K = 6$  for the same image #58, using MCODs for the detection criterion, undamaged areas were detected (Figure 13(a)). If only the gray level residuals were considered, a fine description of the cracked state was observed in the damage field (Figure 13(b)). Contrary to the cases with  $K = 3$ , the coupled criterion now seems to erase some small aspects of the cracked network seen in the gray level residuals, when comparing Figures 13(b, c), yet both led to very similar damage fields.



(a)



(b)

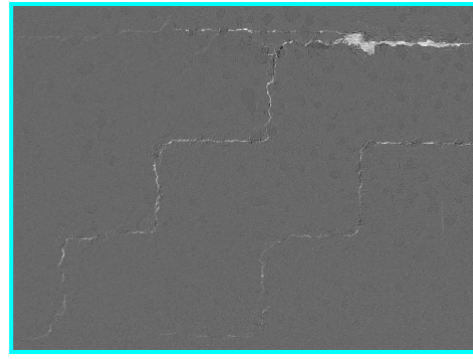


(c)

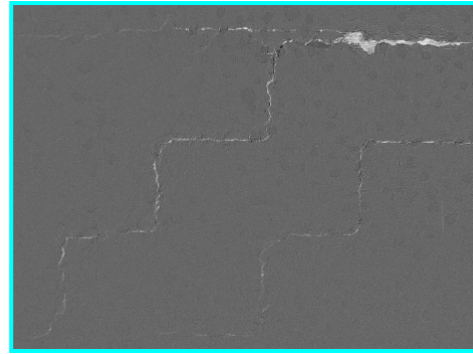
**Figure 13.** Damaged elements for deformed image #58 using as detection criterion only MCODs (a), gray level residuals (b), or both (c), all with  $K = 6$

A zoomed region (bottom left of the ROI, see Figure 4(a)) of image #19 was selected to distinguish the previous results. This image was the first one for which the global gray level residual increased beyond its baseline (or noise floor level, see Figure 7(b)), namely, where higher gray levels (*i.e.*, cracks) occurred. Figure 14(a, b) displays the residuals when  $K = 6$  and using only the gray level (Figure 14(a)) or the coupled criterion (Figure 14(b)). In both cases, the crack network is visible, and matches better the damage pattern when only gray level residuals are used as detection quantity (Figure 14(c)). Part of the damage was not detected by the coupled criterion (Figure 14(d)). Therefore, the choice

$K = 6$  was made and using only the gray level residual was validated. It was the only one selected in the following analyses.



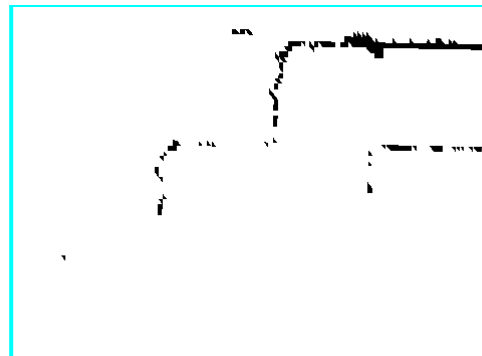
(a)



(b)



(c)



(d)

**Figure 14.** Detail (see Figure 4(a)) of the gray level residual for the DIC analysis of image #19 using  $K = 6$  and only the gray level residual as criterion (a) or the coupled criterion (b). (c, d) Corresponding damage fields.

## Results and Discussion

The following section mostly focuses on MCOd data. The way they were computed, namely, from the maximum eigen strains averaged over each element, they will inform on locations where the cracks were open or sliding (*i.e.*, only positive MCOdS are shown).

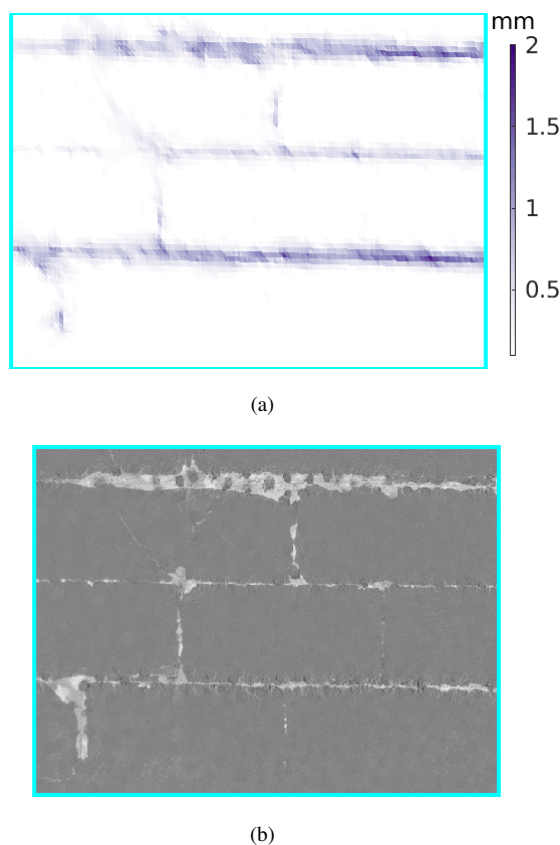
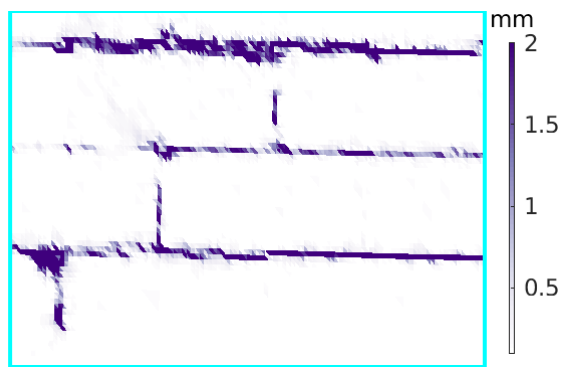


**Figure 15.** Details (see Figure 4(a)) of (a) MCOd and (b) gray level residual fields for image #58 using a fine uniform mesh.

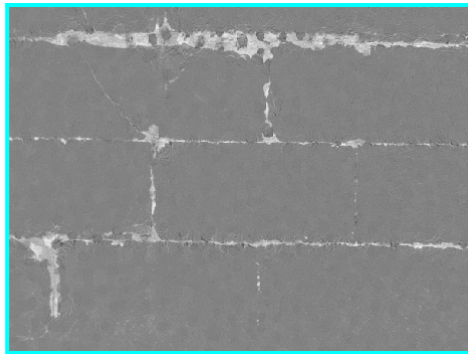
### Comparisons with simpler DIC implementations

If no adaptive mesh or damage was considered, an analysis with a very fine mesh with mechanical regularization would provide the best description of the displacement field in such challenging case. The results obtained with a uniform mesh with an element size of 9 px, which was the smallest in the adapted mesh, are first discussed. This mesh was created using the same element subdivision routine, but choosing all elements to be subdivided at each step. The MCOd field for image #58 is shown in Figure 15(a) for a zoomed area. The field was blurred due to the mechanical regularization, which spread the strains over few elements. Its corresponding gray level residual map is shown in Figure 15(b). Although a proper description of the crack network is observed, there are interpolation errors close to the horizontal cracks, which were created by enforcing the continuity and mechanical admissibility of displacements.

Similar results are reported in Figure 16 with the adapted mesh (with  $k = 3$ ). The DIC analyses were conducted with damage based on the gray level residual (with  $K = 6$ ). In the MCOd field (Figure 16(a)), the localization of the cracks is visible in single elements. Even though the dynamic range of the color map was saturated at openings greater than 2 mm (for comparison purposes with the uniform mesh), local openings of up to 10 mm were captured for some elements. This better description is also perceptible in the gray level residuals (Figure 16(b)) in which, for smaller openings, they are concentrated in a single pixel line. It is worth noting that for this small ROI, the adapted mesh had about 30% fewer elements than the uniform mesh, while still yielding a better description of the underlying phenomenon.



(a)



(b)

**Figure 16.** Details (see Figure 4(a)) of (a) MCOD and (b) gray level residual maps for image #58 using the adapted mesh.

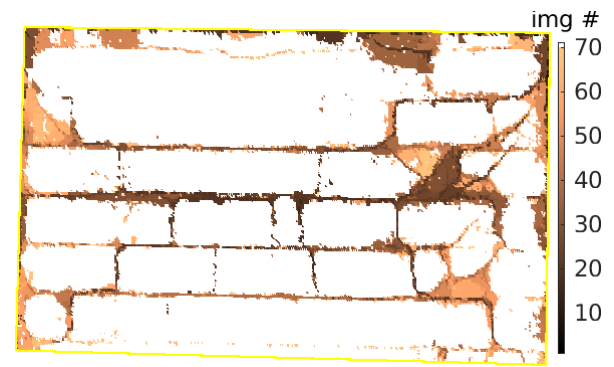


**Figure 17.** Map of first image for which elements were damaged. If damage never occurred, the element remains white.

### Crack network development

The following procedure aims to have a spatial and temporal description of damage development, which is summarized in Figure 17. The color rendering of each element represents the image when damage initiated (*i.e.*, when the threshold was surpassed). If the element is white, it means that it remained undamaged for the whole analysis. Many undamaged regions are observed between cracked regions. Damage initiated in the central horizontal region and along the main diagonals up to image #19. By reaching the maximum load, more horizontal cracked regions were formed, and damage grew toward the outside frame. The bigger damaged regions were related to a sudden fall of the cladding.

The same type of map was drawn using only the elements that were damaged at the peak loads for positive (Figure 18(a)) or negative (Figure 18(b)) applied displacements. Apart from the previous conclusion pointing out that damage started in the center and grew outward, a first diagonal band is seen in both cases, which was aligned along the loading direction applied at the top part of the wall. Then, beyond the maximum force, other horizontal bands appeared, some for the very last images (*e.g.*, see top of Figure 18(b)). These maps provide interesting data to validate damage models.

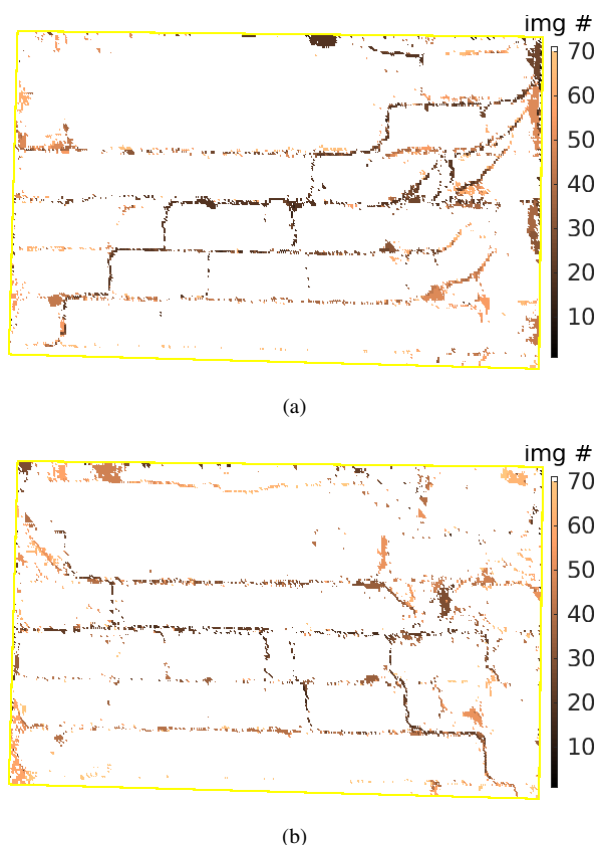


**Figure 18.** Map of first image for which elements were damaged in the peak loads for positive (a) and negative (b) applied displacements (see Figure 4(b)). If damage never occurred, the element remains white.

For a finer description of crack initiation, it is proposed to further investigate both series of images highlighted in the loading history displayed in Figure 19, for maximum positive or negative strokes where softening occurred. The range for the color map was set small in order to highlight the damage pattern (*i.e.*, MCOB levels less than 1 px or 0.8 mm).

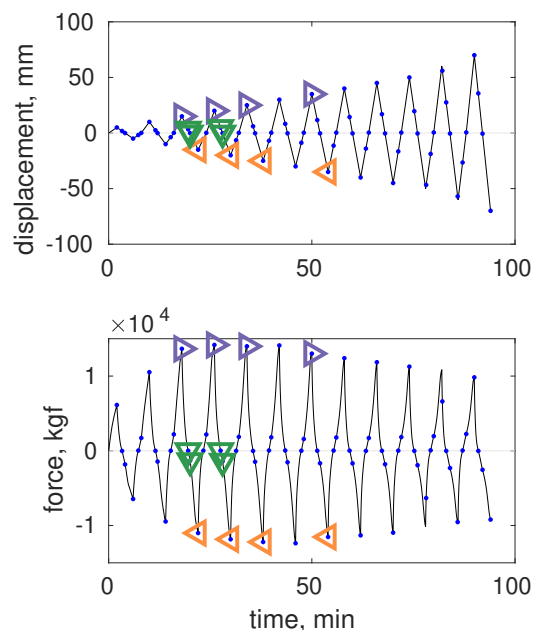
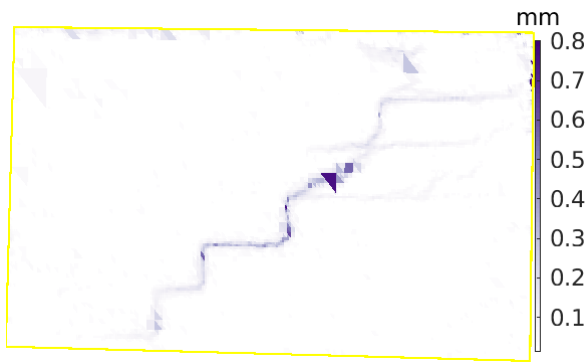
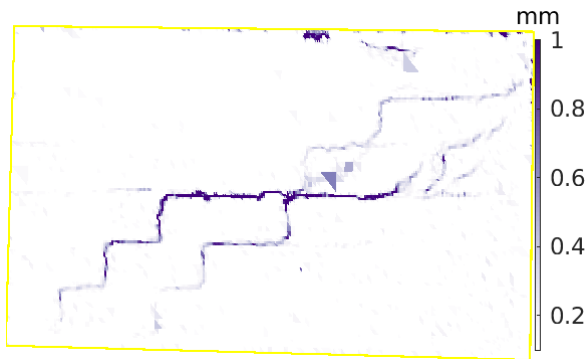


**Figure 19.** Stroke and force histories. The blue dots depict image acquisitions, and the triangles the series of images studied for crack initiation for positive (in purple, images #13, 19, 25, and 37) or negative (in orange, images #16, 22, 28, and 40) prescribed displacements. To analyze the activation / deactivation of crack systems, additional frames were considered (in green, images #14, 15, 20, and 21).

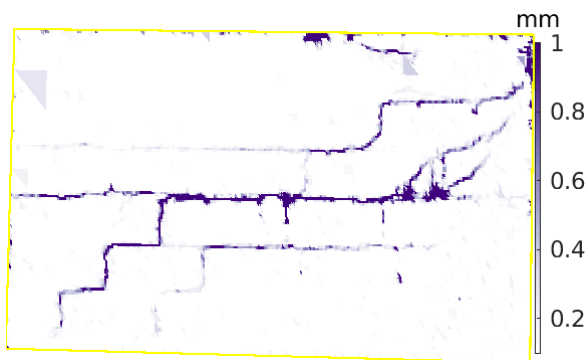
MCOB fields are displayed in Figure 20 for the time steps related to damage initiation for positive strokes. The results are first shown for image #13 (Figure 20(a)), which was the first one where cracks appeared in the gray level residual map even though not yet perceptible in the global residual (Figure 7(b)). A first zigzagged diagonal pattern is observed with very small openings in the top right part. On the following cycle (image #19), two diagonal bands are observed (Figure 20(b)). For image #25, three horizontal bands became more prominent (Figure 20(c)), and a fourth one developed two cycles after (at image #37, see Figure 20(d)). The large damaged zones are due to cladding loss.



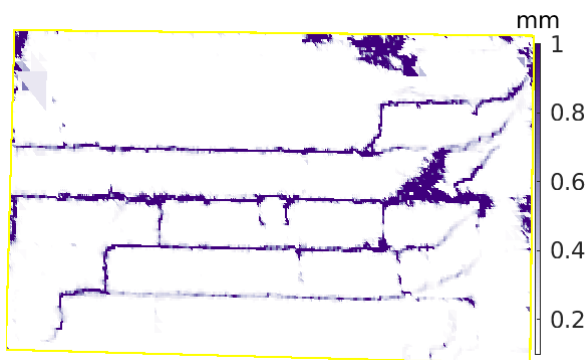
(a)



(b)



(c)

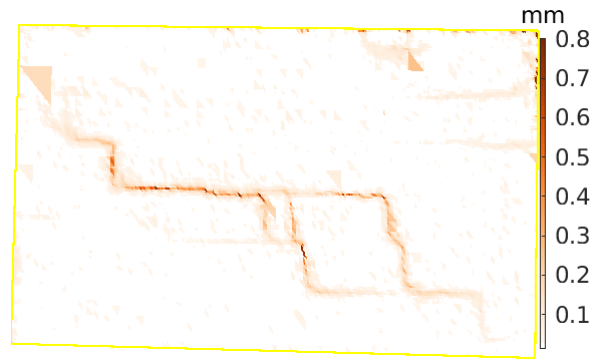


(d)

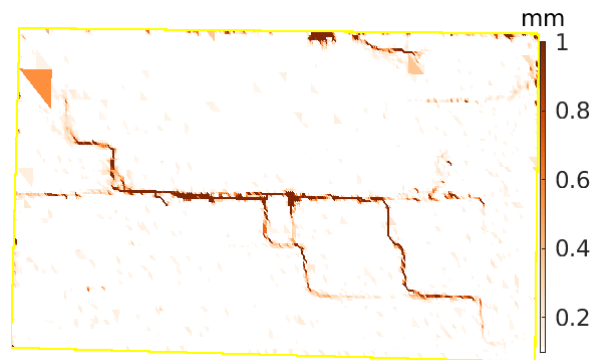
**Figure 20.** MCOD fields for images #13 (a), 19 (b), 25 (c), and 37 (d), at peak loads of positive displacement (Figure 19)

Similar trends are observed for MCOD fields associated with negative displacement peaks (Figure 21). One main

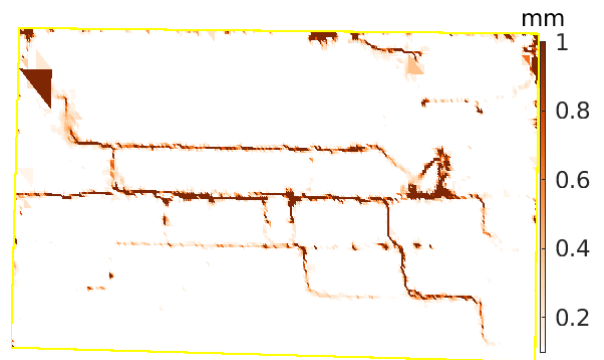
diagonal band first formed at image #16 (Figure 21(a)) with some bifurcation at the bottom right.



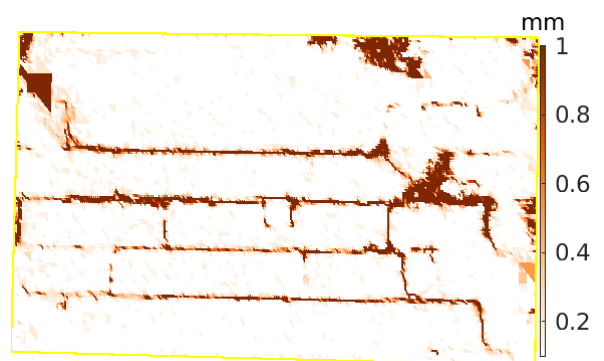
(a)



(b)



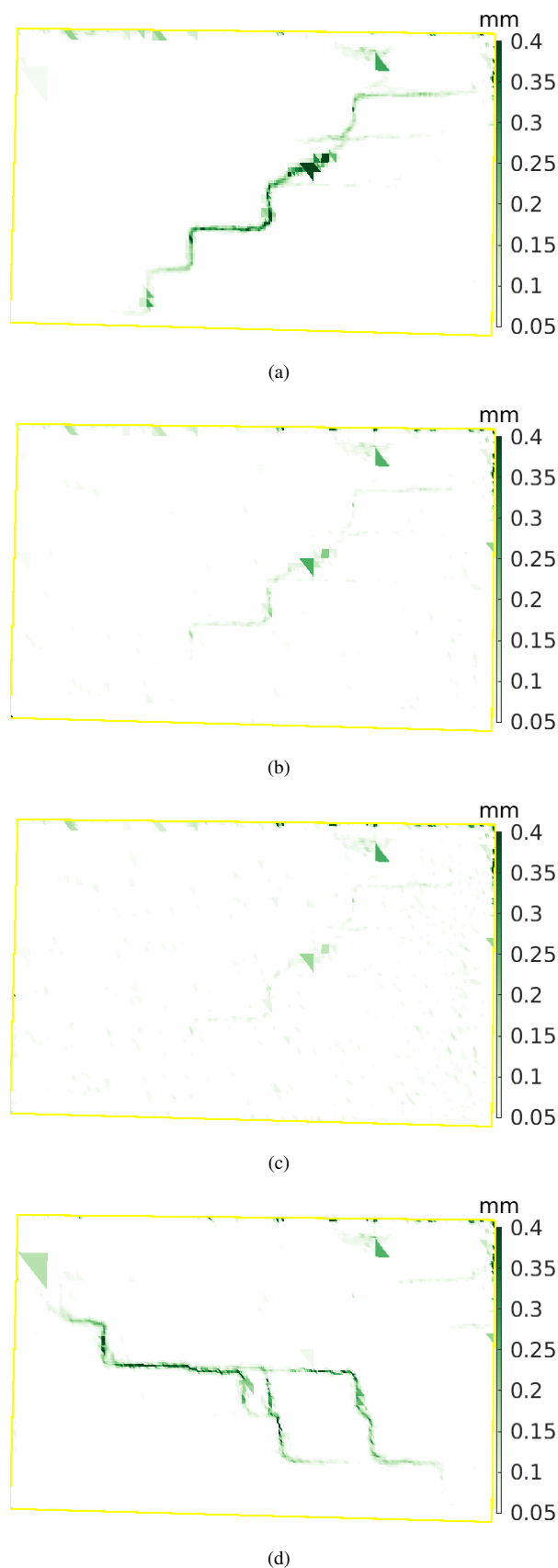
(c)



(d)

**Figure 21.** MCOD fields for images #16 (a), 22 (b), 28 (c), and 40 (d), at peak loads of negative strokes (Figure 19)

Part of the openings seen at the top right for image #13 (Figure 20(a)) remained, which indicated that the cracks did not fully close upon load reversal. On the next cycle (image #22), the development of a big horizontal crack occurred at mid-height (Figure 21(b)). For image #28, an additional diagonal band appeared on the right side and two more horizontal ones (Figure 21(c)). A fourth horizontal crack was then created two cycles later (image #40, see Figure 21(d)).



To further investigate the crack system development upon load reversals, two intermediate MCOD fields are also shown in Figure 22 (*i.e.*, images #14 and 15, see green triangles in Figure 19) in addition to images #13 and 16 for comparison purposes. The result of the first image (Figure 22(a)) was already reported (Figure 20(a)) but with a higher dynamic range compared to the present one (*i.e.*, 0.4 mm or  $\approx 0.5$  px for the latter). The highest MCOD levels occurred in the central part of the wall. Figure 22(b) corresponds to the unloading stage with zero applied force. The zigzagged crack had essentially closed with very limited residual opening. It further closed when the applied displacement was equal to zero (Figure 19(c)). The second system of zigzagged cracks was formed for image #16 (Figure 22(d)). The highest MCOD levels again took place in the central part of the wall. In this first regime, cracking that was induced by the first loading direction was deactivated as soon as the second one was activated and vice-versa. For the sake of conciseness, the next cycle is not reported. However, all the trends shown Figure 22 were identical, except the MCOD levels that increased because of higher stroke.

**Figure 22.** MCOD fields for images #13 (a), 14 (b), 15 (c), and 16 (d). It is worth noting that the dynamic range was lowered in comparison to Figure 20

The same analysis was performed for the fourth cycle. Two intermediate MCOD fields are also shown in Figure 23 (*i.e.*, images #20 and 21, see green triangles in Figure 19) in addition to images #19 and 22 for comparison purposes. The result of the first image (Figure 23(a)) was already reported (Figure 20(b)) but with a different dynamic range. The highest MCOD levels were significantly higher in the central part of the wall. Figure 23(b) corresponds to the unloading stage with zero applied force. Many of the zigzagged cracks had essentially closed (as in the previous case, see Figure 22). However, the horizontal crack remained open, presumably due to friction. The zigzagged cracks further closed when the applied displacement was equal to zero (Figure 19(c)) and the horizontal crack was still substantially open. Conversely, the second system of zigzagged cracks that was fully open for image #22 (Figure 23(c)) was still mostly closed. The second system of zigzagged cracks opened again for image #22 (Figure 23(d)) but most of the MCOD took place in the central part of the wall and for the horizontal crack. Contrary to the previous results (Figure 22), the horizontal crack experienced much higher MCOD levels.

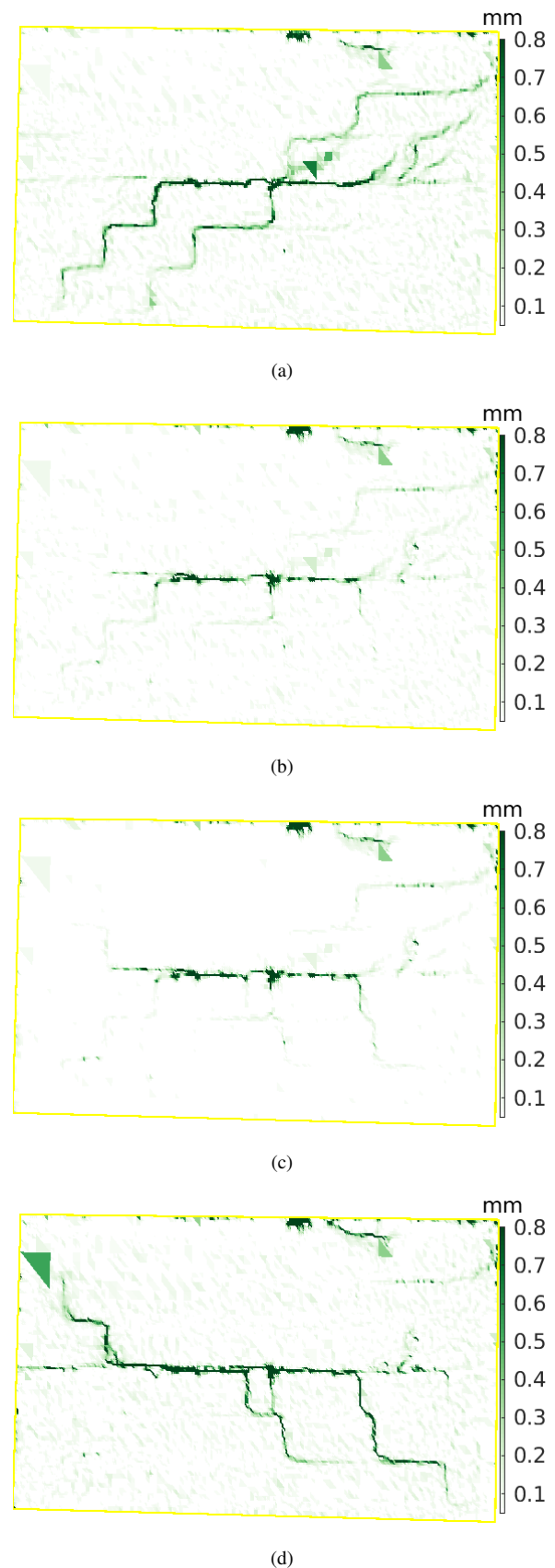


**Figure 23.** MCOD fields for images #19 (a), 20 (b), 21 (c), and 22 (d). Sub-figures (a) and (d) were already reported with different dynamic ranges in Figures 20(b) and 21(b), respectively.

### Macroscopic damage quantification

One first quantification of macroscopic damage is shown in Figure 24, by considering the mean shear strain of the whole ROI and comparing to its evolution with the applied forces. The mean shear strain was very low for the first images, and as it increased, the force started to decay (in absolute value). The red circles depict the first 19 images (up to the peak load), which are the same highlighted inside the red box in Figure 25. It is interesting to note that from the previous results, it was concluded that damage had already initiated before reaching the ultimate force.

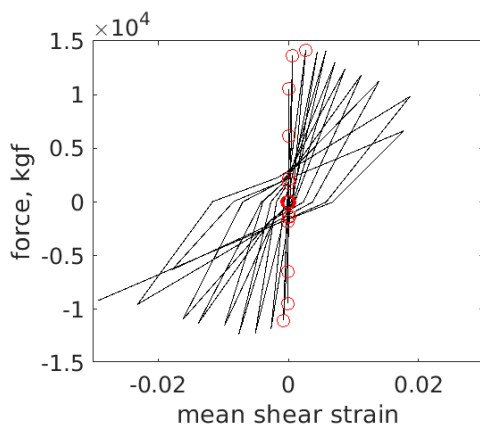
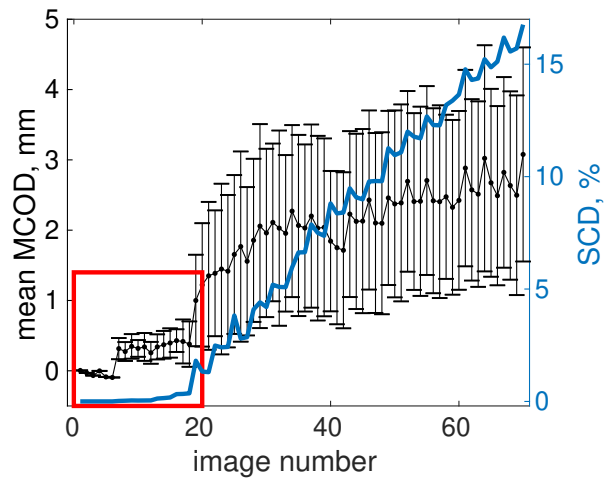


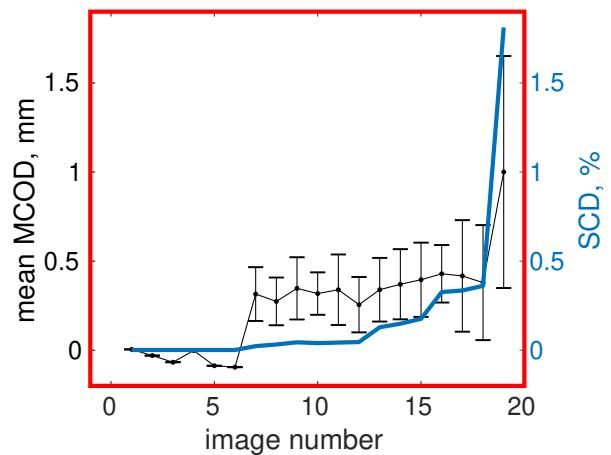
**Figure 24.** Measured force as a function of mean shear strain calculated over the whole ROI. The red circles depicts all the images up to the peak load (image #19).

Even if the previous discussions already gave a lot of insight into crack initiation and propagation in the infill, the selected ranges did not allow the crack openings to be fully quantified. Such type of information was obtained from the mean MCOD in damaged elements and the Surface Crack Density (SCD), calculated as the damaged area divided by the ROI area. Both quantities are displayed in Figure 25. Prior to image #19, very few elements were damaged, and the damaged ones had a very low MCOD (*i.e.*, on average less than 0.4 mm or 0.5 px). A sudden increase in mean MCOD (from 0.4 mm to 1 mm) is observed after image #19, which then continues to grow stably but at a slower rate up to the end of the test. Once the SCD started to grow (at image #19), it increased linearly up to the end. This trend corresponds to the existence of two different mechanisms (Figures 20 and 21). First, from images #7 to #18, damage developed as diagonal bands with essentially constant mean MCOD of  $\approx 0.4$  mm and gradual increase of the number of damaged elements (Figure 25(b)). Second, horizontal bands were formed with the SCD gradually increasing with

fluctuations associated with the cyclic nature of the applied load (Figure 4(b)). It was accompanied by an initially fast increase of mean MCOD, which then slowed down.



(a)



(b)

**Figure 25.** (a) Average MCODs of damaged elements and Surface Crack Density as functions of image number, and (b) zoom for the first 19 images (red box of sub-figure (a)). The length of the error bars corresponds to the standard deviation of MCODs.

To further investigate the oscillations observed in Figure 25, both mean MCOD and SCD are shown as functions of the minimum (Figure 26(a)) or maximum (Figure 26(b)) shear strain per cycle, depending whether the prescribed displacement was negative or positive. The increasing trend in both cases highlights the fact that damage mostly developed on the envelope of the loading history, while the intermediate points on loading reversal were related to closure of one crack system and opening of the other one.

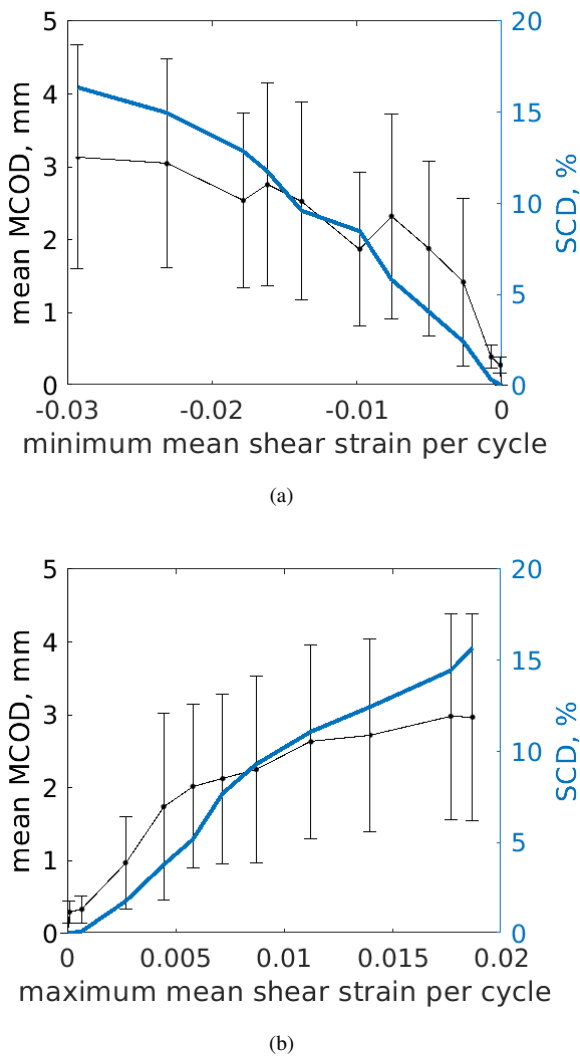


**Figure 26.** Average MCODs of damaged elements and Surface Crack Density as functions of minimum (a) and maximum (b) mean shear strain for each cycle of the experiment, depending whether the prescribed displacement was negative or positive. The length of the error bars corresponds to the standard deviation of MCODs

Compared to the results reported on crack networks upon curing MgO-containing refractory,<sup>48</sup> the previous trends are totally different. Desiccation induced a very fast development of damage on external surfaces (*i.e.*, the SCD increased very quickly and saturated early on) whereas the mean MCOD increased in a more gradual way as the cracks were propagating normal to the cracked surface within the refractory bulk, thereby further opening their observed mouths. In the present case, it is believed that the crack patterns were very similar on both lateral surfaces as the thickness of the wall was the smallest of all dimensions by more than one order of magnitude and the applied loading did not allow for crack arrest in the thickness.

Such observations highlight the benefits of considering both MCOD and SCD data instead of only one of them.

## Conclusion

Concrete masonry blocks were used to build a real size wall (*i.e.*,  $1.75 \times 2.65 \text{ m}^2$ ), which was submitted to cyclic simple shear to mimic seismic motions. Digital Image Correlation (DIC) analyses were carried out to investigate and quantify the development of cracks in the wall. New DIC strategies (*i.e.*, mechanical regularization, mesh adaption, and damage) were combined to deal with the challenge of following very small cracks in a big wall whose cladding was also damaged during the loading history. All the analyses relied on the evaluation of measurement uncertainties to set the detection thresholds.

Mechanical regularization (with a length of 50 px or 39.5 mm) reduced the uncertainty of the Mean Crack Opening Displacement (MCOD) per element by one order of magnitude. The MCOD uncertainty, which was assessed according to element sizes, was used as a criterion for mesh adaption. This strategy induced localized refinements of the mesh in damaged elements with higher MCOD values in the wall infill. After combining mechanical regularization and mesh adaption, heterogeneous gray level residuals were observed around cracks. This effect was indicative of an excess of regularization in those elements, since mechanical regularization filters out high displacement gradients in elements to their neighbors. The last added strategy was a damage criterion, which reduced the regularization weight in specific elements by degrading their rigidity. Three damage detection criteria were compared. One was related to MCODs (already used as mesh adaption criterion), another one element-wise gray level residuals, and a combination of both. In the present case, the criterion only based on gray level residuals showed a better description of the damage pattern.

After careful setting of the DIC parameters, the crack network could be investigated thanks to mean crack opening displacement (MCOD) and gray level residual fields. Spatial and temporal descriptions of damage growth and deactivation were extracted. First, diagonal and zigzagged bands (*i.e.*, diagonal cracking) initiated up to the maximum force. Because of the cyclic nature of the loading history, two different networks developed. Then, a second set of horizontal bands (*i.e.*, sliding shear) followed, which led to a gradual softening of the applied force. At the global level

of the infill, two complementary parameters were defined, namely, the surface crack density and average MCOD. Their variations were very different for the two damage mechanisms. For the first damage regime, the MCODs remained very small (*i.e.*, on average on the order of 0.4 mm) and the zigzagged cracks fully activated/deactivated upon load reversal. Conversely, for the second damage regime, significantly higher MCOD levels were observed (on average from 1 to 3 mm) essentially on horizontal cracks. The number of damaged elements also increased very significantly. Such quantitative analyses were not performed in an earlier study on various infilled configurations<sup>12</sup> (among which the test investigated herein), which focused on damage mechanisms and on the final failure mode.

To quantify crack opening displacement fields, the maximum principal strain was utilized at the element level (*i.e.*, microscale). Such indicator does not distinguish simultaneous mode I and II contributions. In the present case, it is believed that such situation did not occur. Had it been the case, directional indicators associated with the block arrangement would have been needed.

For the DIC analyses, the chosen regularization length and thresholds for adapting the mesh or setting damage (*i.e.*, parameters  $k$  and  $K$ ) may be further investigated for a broader range of combinations. Brightness and contrast corrections<sup>58</sup> could also be applied to improve the description in the regions where cladding fell off and for describing changes in illumination. Different experimental setups and loading protocols could be tested using such methodology. More cameras may be added for stereocorrelation purposes,<sup>15</sup> in which the out-of-plane motions would also be measurable. Last, these full-field analyses provide very rich data sets that can be used for comparisons to numerical simulations of full scale structural elements to validate damage models at various scales.

### Declaration of conflicting interests

The author(s) declared no potential conflicts of interest with respect to the research, authorship, and/or publication of this article.

### Funding

The experiment discussed in this paper was conducted in the course of an investigation sponsored by FONACIT-ECOS NORD and CDCHT-UCLA. The present study was supported in part by the Coordenação de Aperfeiçoamento de Pessoal de Nível Superior -

Brasil (CAPES) - Finance Code 001, and grants #2018/23081-0 and #2021/09238-6, São Paulo Research Foundation (FAPESP).

### References

1. Janaraj T and Dhanasekar M. Finite element analysis of the in-plane shear behaviour of masonry panels confined with reinforced grouted cores. *Construction and Building Materials* 2014; 65: 495–506.
2. Yacila J, Camata G, Salsavilca J et al. Pushover analysis of confined masonry walls using a 3d macro-modelling approach. *Engineering Structures* 2019; 201: 109731.
3. Ahmed A and Shahzada K. Seismic vulnerability assessment of confined masonry structures by macro-modeling approach. *Structures* 2020; 27: 639–649.
4. Korswagen PA, Longo M and Rots JG. High-resolution monitoring of the initial development of cracks in experimental masonry shear walls and their reproduction in finite element models. *Engineering Structures* 2020; 211: 110365.
5. Asociación Colombiana de Ingeniería Sísmica, Título A - Requisitos Generales de Diseño y Construcción Sismo Resistente, Nsr-10, vol. Título A, pp. 1–174, 2010.
6. Asociación Colombiana de Ingeniería Sísmica, Título E - Casas de uno y dos pisos, Nsr-10, pp. 1–46, 2010.
7. SENCICO, NTE E.030 de diseño sismorresistente de edificios del Perú, 2003.
8. Ministerio de Vivienda, Norma Técnica E.070. Albañilería, Rne, pp. 297-299, 2006.
9. FODENORCA, Construcciones sismorresistentes. Parte 1: Requisitos (2da. Revisión), 2019.
10. FODENORCA, Análisis, diseño y construcción de edificaciones de mampostería estructural, vol. 8, no. 5, Caracas, 2019.
11. Asteris PG, Antoniou ST, Sophianopoulos DS et al. Mathematical Macromodeling of Infilled Frames: State of the Art. *Journal of Structural Engineering* 2011; 137(12): 1508–1517.
12. Guerrero N, Martinez M, Picon R et al. Experimental analysis of masonry infilled frames using digital image correlation. *Materials and structures* 2014; 47(5): 873–884.
13. Asteris P, Kyriazopoulos A and Vouthounis P. The state-of-the-art in infilled frames numerical models. In *Proceedings of the Structural Engineering World Congress (SEWC2002)*, volume Paper No. T1-2-c2. Yokohama (Japan).
14. Petry S and Beyer K. Limit states of modern unreinforced clay brick masonry walls subjected to in-plane loading. *Bulletin of earthquake engineering* 2015; 13(4): 1073–1095.

15. Sutton M. Computer vision-based, noncontacting deformation measurements in mechanics: A generational transformation. *Appl Mech Rev* 2013; 65(AMR-13-1009): 050802.
16. Küntz M, Jolin M, Bastien J et al. Digital image correlation analysis of crack behavior in a reinforced concrete beam during a load test. *Canad J Civil Eng* 2006; 33: 1418–1425.
17. Mousa MA, Yussof MM, Udi UJ et al. Application of digital image correlation in structural health monitoring of bridge infrastructures: A review. *Infrastructures* 2021; 6(12): 176.
18. Tung S, Shih M and Sung W. Development of digital image correlation method to analyse crack variations of masonry wall. *Sadhana* 2008; 33: 767–779.
19. Bui TT and Limam A. Out-of-plane behaviour of hollow concrete block masonry walls unstrengthened and strengthened with cfrp composite. *Composites Part B: Engineering* 2014; 67: 527–542.
20. Herbert D, Gardner D, Harbottle M et al. Uniform lateral load capacity of small-scale masonry wall panels. *Materials and Structures* 2014; 47: 805–818.
21. Vanniamparambil PA, Bolhassani M, Carmi R et al. A data fusion approach for progressive damage quantification in reinforced concrete masonry walls. *Smart Materials and Structures* 2013; 23(1): 015007.
22. Salmanpour AH, Mojsilović N and Schwartz J. Displacement capacity of contemporary unreinforced masonry walls: An experimental study. *Engineering Structures* 2015; 89: 1–16.
23. Casolo S, Biolzi L, Carvelli V et al. Testing masonry blockwork panels for orthotropic shear strength. *Construction and Building Materials* 2019; 214: 74–92.
24. Stazi F, Serpilli M, Chiappini G et al. Experimental study of the mechanical behaviour of a new extruded earth block masonry. *Construction and Building Materials* 2020; 244: 118368.
25. Torres B, Varona FB, Baeza FJ et al. Study on retrofitted masonry elements under shear using digital image correlation. *Sensors* 2020; 20(7): 2122.
26. Elghazouli A, Bompa D, Mourad S et al. In-plane lateral cyclic behaviour of lime-mortar and clay-brick masonry walls in dry and wet conditions. *Bulletin of Earthquake Engineering* 2021; 19: 5525–5563.
27. Howlader M, Masia M and Griffith M. Digital image correlation for the analysis of in-plane tested unreinforced masonry walls. *Structures* 2021; 29: 427–445.
28. Ghorbani R, Matta F and Sutton M. Full-field deformation measurement and crack mapping on confined masonry walls using digital image correlation. *Experimental Mechanics* 2015; 55: 227–243.
29. Calderón S, Sandoval C, Araya-Letelier G et al. Quasi-static testing of concrete masonry shear walls with different horizontal reinforcement schemes. *Journal of Building Engineering* 2021; 38: 102201.
30. Serpilli M, Stazi F and Lenci GC. Earthen claddings in lightweight timber framed buildings: An experimental study on the influence of fir boards sheathing and gfrp jacketing. *Construction and Building Materials* 2021; 285: 122896.
31. Bolhassani M, Hamid A, Rajaram S et al. Failure analysis and damage detection of partially grouted masonry walls by enhancing deformation measurement using dic. *Engineering Structures* 2017; 134: 262–275.
32. Fedele R, Scaioni M, Barazzetti L et al. Delamination tests on cfrp-reinforced masonry pillars: Optical monitoring and mechanical modeling. *Cement and Concrete Composites* 2014; 45: 243–254.
33. Didier M, Abbiati G, Hefti F et al. Damage quantification in plastered unreinforced masonry walls using digital image correlation. In *10th Australasian masonry conference*. pp. 14–18.
34. Korswagen P, Longo M, Meulman E et al. Crack initiation and propagation in unreinforced masonry specimens subjected to repeated in-plane loading during light damage. *Bulletin of Earthquake Engineering* 2019; 17: 4651–4687.
35. Calderón S, Sandoval C, Inzunza E et al. Influence of a window-type opening on the shear response of partially-grouted masonry shear walls. *Engineering Structures* 2019; 201: 109783.
36. Meriggi P, Caggegi C, Gabor A et al. Shear-compression tests on stone masonry walls strengthened with basalt textile reinforced mortar (trm). *Construction and Building Materials* 2022; 316: 125804.
37. Rezaie A, Achanta R, Godio M et al. Comparison of crack segmentation using digital image correlation measurements and deep learning. *Construction and Building Materials* 2020; 261: 120474.
38. Gehri N, Mata-Falcón J and Kaufmann W. Automated crack detection and measurement based on digital image correlation. *Construction and Building Materials* 2020; 256: 119383.
39. Besnard G, Hild F and Roux S. “Finite-element” displacement fields analysis from digital images: Application to Portevin-Le Chatelier bands. *Exp Mech* 2006; 46: 789–803.
40. Hild F, Bouterf A and Roux S. Damage Measurements via DIC. *International Journal of Fracture* 2015; 191(1-2): 77–105.
41. Sciuti VF, Vargas R, Canto RB et al. Pyramidal Adaptive Meshing for Digital Image Correlation Dealing With Cracks.

- Engineering Fracture Mechanics* 2021; 256: 107931.
42. Hild F and Roux S. Comparison of local and global approaches to digital image correlation. *Experimental Mechanics* 2012; 52(9): 1503–1519.
  43. Standardization, Good Practices, and Uncertainty Quantification Committee. A Good Practices Guide for Digital Image Correlation. International Digital Image Correlation Society (iDICs), 2018. URL [idics.org/guide/](http://idics.org/guide/).
  44. EN 4861, Aerospace series - Metrological assessment procedure for kinematic fields measured by digital image correlation. European Committee for Standardization (CEN), 2020.
  45. Sciuti VF, Hild F, Pandolfelli VC et al. Digital image correlation applied to *in situ* evaluation of surface cracks upon curing of MgO-containing refractory castables. *Journal of the European Ceramic Society* 2020; .
  46. Guerrero N. *Análisis Teórico-Experimental del Daño y del Pandeo Local en Estructuras de Ingeniería Civil (in Spanish)*. PhD Thesis, University of Los Andes, Venezuela, 2007.
  47. Leclerc H, Neggers J, Mathieu F et al. Correli 3.0, 2015. IDDN.FR.001.520008.000.S.P.2015.000.31500.
  48. Sciuti V, Hild F, Pandolfelli V et al. Digital Image Correlation applied to *in situ* evaluation of surface cracks upon curing of MgO-containing refractory castables. *Journal of the European Ceramic Society* 2021; 41(1).
  49. Vakulenko A and Kachanov M. Continuum theory of medium with cracks. *Isv AN SSSR, Mekh Tverdogo Tela* 1971; 4: 159–166.
  50. Réthoré J, Roux S and Hild F. An extended and integrated digital image correlation technique applied to the analysis fractured samples. *Eur J Comput Mech* 2009; 18: 285–306.
  51. Tomičević Z, Hild F and Roux S. Mechanics-aided digital image correlation. *J Strain Analysis* 2013; 48: 330–343.
  52. Claire D, Hild F and Roux S. A finite element formulation to identify damage fields: The equilibrium gap method. *Int J Num Meth Engng* 2004; 61(2): 189–208.
  53. Mendoza A, Neggers J, Hild F et al. Complete mechanical regularization applied to digital image and volume correlation. *Computer Methods in Applied Mechanics and Engineering* 2019; 355: 27–43.
  54. Fries TP, Byfut A, Alizada A et al. Hanging nodes and xfem. *International Journal for Numerical Methods in Engineering* 2011; 86(4-5): 404–430.
  55. Hild F, Raka B, Baudequin M et al. Multi-scale displacement field measurements of compressed mineral wool samples by digital image correlation. *Appl Optics* 2002; IP 41(32): 6815–6828.
  56. Hild F and Roux S. Digital image correlation. In Rastogi P and Hack E (eds.) *Optical Methods for Solid Mechanics. A Full-Field Approach*. Weinheim (Germany): Wiley-VCH, pp. 183–228.
  57. Sciuti VF, Vargas R, Canto RB et al. Pyramidal adaptive meshing for Digital Image Correlation dealing with cracks. *Engineering Fracture Mechanics* 2021; 256: 107931.
  58. Sciuti VF, Canto RB, Neggers J et al. On the benefits of correcting brightness and contrast in global digital image correlation: Monitoring cracks during curing and drying of a refractory castable. *Optics and Lasers in Engineering* 2020; 136: 106316.

## Appendix: DIC parameters

**Table 1.** DIC hardware parameters

Camera	Sony Cyber-shot DSC-R1
Definition	2592 × 3888 px
Color filter	Bayer
Gray Levels amplitude	8 bits
Lens	Zeiss 24-120 mm
Aperture	f/5.6
Field of view	2.05 × 3.07 m <sup>2</sup>
Image scale	790 μm/px
Stand-off distance	≈ 3.5 m
Image acquisition rate	manual
Exposure time	15 ms
Patterning technique	brushed paint
Pattern feature size <sup>#</sup>	18 pixels (B/W)

<sup>#</sup>evaluated as full width at half maximum of autocorrelation function

**Table 2.** DIC analysis parameters

DIC software	Correli 3.0 <sup>47</sup>
Image filtering	none
Shape functions	linear (T3)
Element length	adapted mesh (Figure 9(b))
Matching criterion	regularized sum of squared differences
Interpolant	cubic
Strain calculation	derivative of shape functions
Regularization length	50 px